

CNWRA *A center of excellence in earth sciences and engineering™*

A Division of Southwest Research Institute®
6220 Culebra Road • San Antonio, Texas, U.S.A. 78228-5166
(210) 522-5160 • Fax (210) 522-5155

November 10, 2005
Contract No. NRC-02-02-012
Account No. 20.06002.01.262

U.S. Nuclear Regulatory Commission
ATTN: Dr. James Rubenstone
Division of High-Level Waste Repository Safety
Office of Nuclear Material Safety and Safeguards
Mail Stop 7 C6
Washington, DC 20555

Subject: Transmittal of requested revision to IM 20.06002.01.262.520

Dear Dr. Rubenstone:

This letter transmits the revised deliverable "Fault and Fracture Characteristics Supporting Gas Permeability Measurements of Bedded Volcaniclastics-Journal Article" (IM 20.06002.01.262.520). Revisions address NRC comments on the revised paper submitted to NRC on 05/28/05. The publication title for this milestone is "Deformation Analysis of Tuffaceous Sediments in the Volcanic Tableland Near Bishop, California, Implications for Permeability." Also attached is NRC Form 390A. This milestone will be submitted for publication in the *Journal of Structural Geology*. Because of standard journal practice, parenthetical English units have not been included in the text.

Current DOE models predict large-scale lateral flow within the Paintbrush nonwelded hydrogeologic unit at Yucca Mountain, Nevada. Our paper examines deformation characteristics within an outcrop of tuffaceous sediments that are exposed stratigraphically below the Bishop Tuff in northern Owens Valley, California. A stress analysis of the deformation characteristics observed in this exposure revealed that low differential stress and a near zero value for the minimum principal stress resulted in shear, tensile, and hybrid failure modes. Deformation in this system likely influences intrinsic permeability both vertically and laterally. Vertical fluid movement is focused down dip and lateral fluid movement is restricted horizontally by faults that form permeability barriers. Influences such as these enhance fluid flow in a direction parallel to the intersection line of conjugate faults. This work provides the structural geologic context for permeability data collected from the same exposure to be discussed in a future milestone.



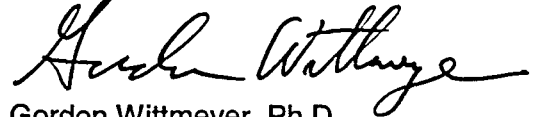
Washington Office • Twinbrook Metro Plaza #210
12300 Twinbrook Parkway • Rockville, Maryland 20852-1606

1 6

Dr. James Rubenstone
November 8, 2005
Page 2

In addition to providing the revised manuscript for your review and approval, the authors have also supplied direct responses to each NRC comment received. If you have any questions concerning this deliverable, please contact me at (210) 522-5082 or Dr. Cynthia Dinwiddie at (210) 522-6085.

Sincerely yours,



Gordon Wittmeyer, Ph.D.
Assistant Director, Earth Sciences

/cp

Attachments (2)

cc:	W. Reamer	E. Collins	P. Justus	W. Patrick	Record Copy B, IQS
	B. Meehan	A. Campbell	J. Pohle	B. Sagar	L. Gutierrez
	D. DeMarco	J. Guttman	R. Fedors	CNWRAs Directors	
	E. Whitt	T. McCartin	A. Fetter	CNWRAs Mgrs.	
	L. Kokajko	J. Bradbury			

Deformation analysis of tuffaceous sediments in the Volcanic Tableland near Bishop, California, and implications for permeability

Journal of Structural Geology

Authors:

Ronald N. McGinnis* E-mail: rmcginnis@swri.org

Alan P. Morris

David A. Ferrill

Cynthia L. Dinwiddie

Center for Nuclear Waste Regulatory Analyses (CNWRA), Geosciences and Engineering Division: Department of Earth, Material, and Planetary Sciences, Geosciences and Engineering Division, Southwest Research Institute, 6220 Culebra Road, San Antonio, TX 78238, USA

*corresponding author: Phone - (210) 522-5825

Fax - (210) 522-5155

E-mail - rmcginnis@swri.org

Keywords:

Volcanic Tableland; Glass Mountain; Tuffaceous Sediments; Stress Analysis; Normal Faults; Extension Fractures; Permeability

Abstract

Small-scale brittle faults and fractures were studied in a cut bank exposure of poorly consolidated tuffaceous sedimentary rock located at the southern erosional boundary of the Volcanic Tableland in Owens Valley, California. This study addresses site-specific variation of fault deformation characteristics where faults cut bedded units with different textures and grain sizes, and provides the structural context for permeability data collected within the exposure. These studies of deformation features and their influence on permeability were motivated by the need to evaluate potential length scales for lateral flow in tephra-fall interbeds at Yucca Mountain, Nevada, a potential site for a high-level waste repository. A 79-m-wide horst developed, in the tuffaceous sedimentary strata of the Volcanic Tableland, is bounded by two faults that account for 75% of the total extension measured in the 110-m-long exposure. Small-displacement (< 20 cm) faults and non-vertical fractures are strongly clustered and positively correlated with larger faults (displacements > 20 cm), whereas vertical fractures are present throughout the exposure. Fracture density (total fracture trace length per unit area) is generally highest in the vicinity of larger faults. The strike trend of all faults and fractures in the exposure is consistent with an average strike azimuth of 355 degrees. Fault zones are characterized by grain size reduction and discrete slip surfaces, the number of which increases with increasing displacement. A stress analysis of this exposure, which was based on tectonic setting and reconstruction of overburden thicknesses, yields a simple history of burial and exhumation under continuous tectonic extension, comparable with that of tuffaceous rocks at Yucca Mountain. We interpret the fault and fracture development of the study area to include shear (faults), hybrid (faults, nonvertical fractures), and tensile (vertical fractures) failure modes under conditions of low overburden stress (< 2.5 MPa). Deformation characteristics such as grain comminution, cementation, and fracture dilation have important effects on groundwater movement that depend strongly on saturation conditions. The intersecting network of faults and fractures in conjunction with stratigraphic layering generates an anisotropic permeability with maximum permeability parallel to fault and fracture strike.

Introduction

The geometry and development of normal fault systems influence intrinsic permeability within various rock types. Prior studies have focused on scaling analyses, segmented fault development, and fault zone deformation mechanisms in various lithologies (Evans, 1990; Dawers et al., 1993; Dawers and Anders, 1995; Pinter, 1995; Knott et al., 1996; Willemse et al., 1996; Willemse, 1997; Ferrill et al., 1998; Ofoegbu and Ferrill, 1998; Ferrill et al., 1999; Morris and Ferrill, 1999; Ferrill and Morris, 2001; Schultz and Fossen, 2002; Stewart and Reeds, 2003; Ferrill et al., 2004). Relatively little work, however, has examined the effects of normal faulting in nonwelded tuffs and tuffaceous sediments on the hydrologic properties in these rock types (Ferrill et al., 2000; Wilson et al., 2003; Evans and Bradbury, 2004; Dinwiddie et al., in review).

This study was motivated by our interest in the deformation characteristics of porous, nonwelded tuff and the potential effects of deformation on its intrinsic permeability. Analog data are of particular interest in the development of a technical basis for evaluating potential length scales for lateral flow within the faulted Paintbrush nonwelded hydrogeologic unit (PTn) at Yucca Mountain, Nevada. Nonwelded tuff units and associated tuffaceous sediments at Yucca Mountain, the site of a potential high-level waste repository, play a prominent role in percolation through the unsaturated zone from the near surface downward to the repository horizon. Yucca Mountain, an east-dipping cuesta associated with primarily west-dipping normal faults, is cut by numerous faults at the map scale and smaller (Day et al., 1998a,b). The gently-dipping PTn overlies the potential repository interval and consists of several nonwelded units, including the vitric

zone at the base of the Tiva Canyon Tuff, pre-Tiva Canyon Tuff bedded tuffs, Yucca Mountain Tuff, pre-Yucca Mountain Tuff, pre-Pah Canyon Tuff bedded tuffs, Pah Canyon Tuff, and the vitric zone at the top of the Topopah Spring Tuff (Moyer et al., 1996). The PTn is assumed to spatially and temporally dampen episodic pulses of meteoric infiltration percolating downward through the overlying Tiva Canyon welded unit. Numerical model simulations (CRWMS M&O, 2000a) suggest that a porous, permeable nonwelded tuff matrix (i.e., PTn) may attenuate rapid, transient fracture flow from the Tiva Canyon; hence, a steady state assumption is often made for unsaturated flow through the fractured tuffs of the potential repository horizon within the Topopah Spring Tuff. Recent modeling (Wu et al., 2000; Bechtel SAIC Company, LLC, 2001) suggests that large-scale lateral flow occurs down-dip along bedding in the PTn, thereby influencing the distribution of the percolation flux to the underlying repository horizon (Bechtel SAIC Company, LLC, 2003a). Estimates of the length over which lateral flow occurs vary from the meter scale to the kilometer scale. While some lateral flow is likely, it is important to determine an appropriate length scale estimate for lateral flow. Large-scale lateral flow could reduce the amount of water that percolates toward waste emplacement drifts by shedding water away from the drifts. Primary heterogeneity or secondary discontinuities (fractures and small faults), however, may inhibit large-scale lateral flow within the PTn and, thus, enhance vertical flow into the Topopah Spring welded tuff below (Fedors and Ferrill, 2002).

Here we examine and characterize the deformation pattern within tuffaceous sediments that are stratigraphically located below the Bishop Tuff in northern Owens Valley, California. The tuffaceous sediments are fluvially reworked volcanic material from the Glass Mountain Complex (Izett et al., 1988) and will be referred to as Crucifix Site sediments throughout this manuscript. The results from this and one other study (performed by Dinwiddie et al., manuscript in preparation) provide insight into the effect that small-scale deformation has on the intrinsic permeability of tuffaceous sediments. This work provides the structural context for permeability data that were collected at this exposure and which will be published in a future paper.

The Crucifix Site exposure is located near the town of Bishop, California (Figure 1a). Owens Valley is bordered by the Sierra Nevada Mountains to the west and the White-Inyo Mountains to the east at the western edge of the Basin and Range province of North America. The valley is a basin that formed by oblique extension during the past 6 m.y. (Lueddecke et al., 1998) and is filled partially by volcanic and sedimentary strata. The northernmost portion of the valley is characterized by a broad plateau called the Volcanic Tableland (Figure 1a), which is capped by the Bishop Tuff. The Tableland is a unique area for study because the moderately welded Bishop Tuff is resistant to erosion and has well-preserved fault-line scarps that record the recent extension of Owens Valley (Figure 1b). This preservation has enabled the systematic investigation of the fault systems within the Volcanic Tableland (Dawers et al., 1993; Dawers and Anders, 1995; Pinter, 1995; Ferrill et al., 1999; Ferrill et al., 2000; Dinwiddie et al., 2002; Evans and Bradbury, 2004; Dinwiddie et al., in review).

Deformation in porous media

Fault zone processes in porous media have been a major topic of research in recent years (Heynekamp et al., 1999; Davatzes and Aydin, 2003; Davatzes et al., 2003; Wilson et al., 2003; Flodin and Aydin, 2004; Odling et al., 2004; Evans and Bradbury, 2004; Dinwiddie et al., in review). Interest in fault zone processes is due, in part, to an increased desire to understand the effect that faults and fractures have on the intrinsic permeability of the subsurface and the importance of this parameter to understanding fluid movement in hydrocarbon reservoirs, aquifers, and the unsaturated zone.

Principal factors that determine fault zone characteristics within various porous lithologies include (i) degree of cementation and postdepositional crystallization (diagenesis), (ii) grain-size distribution, and (iii) clay content. The greater the degree of cementation, or welding in the case of ignimbrites, and postdepositional crystallization, the more likely it is that ash-dominated ignimbrites will deform by fracturing rather than by deformation band formation (i.e., zones in which grain-size and pore volume reduction accommodates displacement) (Wilson et al., 2003). In poorly lithified sandstones, fault zone width and complexity are greater in coarser-grained beds than in finer-grained beds (Heynekamp et al., 1999). Deformation in porous sandstones (18–25% porosity) tends to evolve from deformation bands at low strain, to fractures and ultimately sheared fractures at higher strains, each later structure overprinting the earlier structures (Davatzes and Aydin, 2003). Siliciclastic rocks commonly contain an array of smaller-displacement shear fractures, including discrete faults and deformation bands, clustered around larger-displacement faults (Odling et al., 2004).

Most deformation features have different permeability characteristics compared to the undeformed protolith. Deformation features (e.g., deformation bands and faults of varying displacements formed in poorly-lithified porous rocks) generally have zones of decreased pore size and permeability with respect to the protolith of clastic rocks. This decrease may be the result of pore-collapse in deformation bands (Wilson et al., 2003), clay-smear, and cataclastic grain-size reduction (Heynekamp et al., 1999). In addition, the clustering of small-scale, permeability-reducing deformation features near larger faults will decrease the overall permeability in the vicinity of such faults (Odling et al., 2004). Overprinting deformation features while strain accumulates can lead to variable permeability characteristics of deformation features over time. For example, exploitation of deformation bands by later slip surfaces will likely increase permeability by creating interconnected fracture porosity (Davatzes and Aydin, 2003).

Geologic and tectonic setting

General area

Northern Owens Valley is a broad, tectonic basin bounded by mountain ranges of pre-Cenozoic metamorphic and granitoid rocks (e.g., Hildreth and Mahood, 1986). Pliocene-Pleistocene volcanic activity in the Owens Valley was followed by Pleistocene valley glaciation that deposited moraines along the margins (Gilbert, 1938). Sporadic flooding episodes from the subsequent melting of the glaciers re-deposited tuffaceous sediments (e.g., Crucifix Site sediments) along the valley floor. Most of Owens Valley south of the Volcanic Tableland is covered with alluvium derived primarily from the Sierra Nevada Mountains and White-Inyo Mountains.

The northernmost part of the Owens Valley is covered by the 0.76 Ma Bishop Tuff, which overlies older morainal and alluvial deposits as well as the Crucifix Site sediments. Gilbert (1938) first recognized that the Bishop Tuff represented a nuée ardente-type pyroclastic flow. The deposition of the Bishop Tuff is significant for this study because although the Crucifix Site sediments are not part of the Bishop Tuff, the original thickness of the tuff sheet produced the maximum lithostatic stress (overburden) experienced by the Crucifix Site strata. Numerous studies have built upon Gilbert's original observations and provided new insights into the eruptive history of the Bishop Tuff and its source at the Long Valley Caldera (Figure 1a) (Bateman, 1965; Sheridan, 1970; Ragan and Sheridan, 1972; Hildreth, 1979; Hildreth and Mahood, 1986; Wilson and Hildreth, 1997, 1998, 2003; Evans and Bradbury, 2004). The Bishop Tuff has an isotopic ($^{39}\text{Ar}/^{40}\text{Ar}$) age of 0.758 ± 0.0018 Ma (Sarna-Wojcicki et al., 2000).

Two separate depositional sequences constitute the Bishop Tuff and both contain several distinct units and facies characteristics (Bateman, 1965; Wilson and Hildreth,

1997). The two sequences are a basal fall-dominated sequence (5–20 m thick) overlain by a much thicker tuff sequence (50–150 m thick). The basal sequence is composed of “hybrid” fall deposits, which show features common to both airfall and surge deposits (Wilson and Hildreth, 1998), and is interpreted to have been deposited by smaller venting episodes from openings in the vicinity of the Long Valley Caldera prior to its collapse (Bateman, 1965; Sheridan, 1970; Hildreth and Mahood, 1986; Wilson and Hildreth, 1997, 1998, 2003). The overlying tuff sequence consists of a nonwelded tuff that grades upward into a moderately welded tuff. This moderately welded tuff constitutes the present surface of the Volcanic Tableland (Wilson and Hildreth, 1997; Evans and Bradbury, 2004).

Initial extension of the Owens Valley began in the Late Miocene and produced westward tilting of the valley floor caused by slip on the Sierra Nevada Mountain frontal fault between 6 and 3 Ma (Lueddecke et al., 1998). At approximately 3 Ma, range-front faulting on the White Mountains frontal fault along the eastern border of the Owens Valley marked a switch from westward to eastward tilting of the valley floor (Lueddecke et al., 1998).

Fault scarps are preserved in the Volcanic Tableland, recording the past 0.76 m.y. of extensional history in the valley. The surface of the Tableland is cut by more than 500 scarps with approximately 300 km of surface trace length. Fault scarps generally exhibit north-south strikes and steep dips to the west and east. The underlying faults are inferred to dip between 70–90° (Bateman, 1965; Dawers et al., 1993; Pinter, 1995). Fault throws range from sub-meter to 140 m (Dawers et al., 1993; Dawers and Anders, 1995; Pinter, 1995; Ferrill et al., 1999; Ferrill et al., 2000), and individual fault-trace lengths range up to 4 km (e.g., Fish Slough fault). Nearly 300 m of cross-valley (E-W) extension (post-Bishop-eruption) has been recorded by fault scarps in the moderately welded Bishop Tuff (Pinter, 1995).

Where the Owens River emerges from the Owens River Gorge at the south end of the Volcanic Tableland, it turns sharply and flows eastward across the Owens Valley (Figure 1a), eroding the southern portion of the Tableland and forming a naturally exposed east-west profile through the sequence called Chalk Bluff (Figure 1b). The Crucifix Site is located toward the east end of Chalk Bluff where tuffaceous sediments (i.e., Crucifix Site sediments) derived from the Glass Mountain volcanic complex are exposed (Figure 1b). Small-scale normal faulting and vertical and conjugate fracturing are preserved in a cut bank exposure along the Chalk Bluff road at the Crucifix Site. The exposure is 110 m long and ranges in height from <1 m at each end to ~20 m near the center (coordinates: UTM NAD 27 Zone 11: E = 373761 m, N = 4142025 m). Faults in this exposure have visible displacements of 1 mm to >4 m and include east- and west-dipping faults that intersect and crosscut each other. The crossing conjugate style of faulting observed at the exposure produces horst and graben features (Ferrill et al., 2000).

Lithostratigraphic detail

Understanding the history of deposition at the Crucifix Site is integral to defining the deformation features in the rock. The following section provides details regarding the stratigraphic evolution and overburden history (Figure 2) that has influenced the deformation observed in the Crucifix Site sediments.

The 20-m-thick exposure of Crucifix Site sediments consists of fluvially reworked ash and pumice beds that are poorly sorted and have variable clast sizes. These sediments originated from the Glass Mountain volcanic complex and are characterized by alternating unconsolidated and consolidated beds that are 20 to 60 cm thick (Izett et al., 1988). The Glass Mountain volcanic complex was a precursor to the Bishop Tuff eruption and represents the first magma erupted from the Long Valley magma chamber (Metz and Mahood, 1985). The Glass Mountain volcanic complex was composed of

high-silica rhyolite lavas that erupted to the northeast of what is now the Long Valley Caldera (Figure 1a) (Metz and Mahood, 1985) approximately 40 km northwest of the Crucifix Site. The mineralogical and chemical compositions of the Crucifix Site sediments are nearly identical to the Bishop Tuff pumice-fall deposits (Izett et al., 1988). Glass Mountain eruptions took place between 2.13 and 0.79 Ma and were never large enough to cause caldera collapse (Metz and Mahood, 1985). The Crucifix Site sediments were transported by Pleistocene-age debris flows, hyper-concentrated flood flows (Smith, 1986), and normal stream flows. This braided fluvial system was sporadic and highly variable in its flow regime with the majority of the sediment load being derived from Glass Mountain volcanic complex rocks. Over a period of almost 1.5 m.y., erosion and structural uplift isolated the sediments from this fluvial system as a localized topographic high. This interpretation is evident from the thinning of the basal fall-dominated Bishop Tuff sequence above the Crucifix Site.

The Bishop Tuff is 48 m thick in the vicinity of the Crucifix Site and is composed of a gradational sequence, nonwelded at the base to moderately welded at the top (Wilson and Hildreth, 1997; Evans and Bradbury, 2004) (Figure 2a). The moderately welded tuff at this location represents the welding maximum for this unit. Based on an analog pyroclastic flow [i.e., Matahina Ignimbrite (Riehle et al., 1995)], the degree of welding observed in the Bishop Tuff near the Crucifix Site suggests that the present thickness represents the lower third of the original tuff sheet thickness (Ross and Smith, 1961; Riehle et al., 1995). Based upon this assumption, the original Bishop Tuff sequence overlying the Crucifix Site would have been approximately 173 m thick and would have graded upward from the moderately welded sequence (welding maximum) at the present surface into nonwelded tuff (Figure 2b). Nonwelded tuff formed at the top and bottom of the Bishop Tuff because the substrate and atmosphere were much cooler than the interior of the sheet (Smith, 1960). A welding maximum formed between the two nonwelded sections where the compaction rate and temperature were highest.

The moderately welded Bishop Tuff exposed at the present day surface is resistant to weathering and has protected the less resistant sequence of the Bishop Tuff and the underlying Crucifix Site sediments from erosion. The nonwelded section that originally lay above the moderately welded sequence was eroded to the present surface by fluvial and eolian processes and by Pleistocene glaciation and subsequent melting (Mayo, 1934). The remaining thickness of the Bishop Tuff overlying the Crucifix Site sediments was further eroded by the downcutting of the Owens River, which left a small river terrace above the Crucifix Site sediments that consists of unconsolidated granite cobbles and gravel derived from the Sierra Nevada Mountains. The Bishop Tuff sequence (~173 m thick), thus, has been completely removed from above the Crucifix Site (Figure 2).

Methodology

The geologic methods used to characterize the faults and fractures in the Crucifix Site sediments include photography; sketch mapping; mapping on exposure photographs; and measuring orientations (strike and dip), fault displacements, fault core thicknesses, and areal fracture densities.

Fault survey

Faults were measured and recorded along a bed-parallel scanline survey that spanned the entire length of the exposure. All faults encountered in the exposure have measurable displacements. Using the right hand rule (where the dip direction is clockwise from the recorded azimuth), true strike and dip, as well as down-dip displacement and fault core thickness perpendicular to dip, were measured and recorded. Slickenlines are not visible on fault surfaces; dip-slip movement is assumed because this

location is in an extensional setting. Only down-dip displacements of ≥ 1 mm were measured (criterion for measuring faults this small were that the displacement had to be greater than aperture). Displacements < 1 mm were difficult or impossible to discern in the friable Crucifix Site sediments.

To characterize strain at the Crucifix Site, the total heave, average extension direction, extension-parallel heave, and total extension were calculated. Fault-parallel displacement measurements from each fault were used to calculate the fault-strike-perpendicular heave. StereoStat™ Version 1.3 (Rockware Inc., 2004) was used to plot the fault pole orientations, and an average fault pole orientation was determined for extension fractures and normal faults. The extension direction is assumed to be perpendicular to the average strike direction and this assumption is used as the basis for calculating the extension-parallel heave component of each fault.

Fracture survey

Fracture data from two relatively well-consolidated beds of fine-grained tuffaceous sediments were measured and recorded for a 15-m-long section in the western part of the exposure. These two beds had also been sampled for *in situ* gas permeability (Dinwiddie et al., 2002), which will be documented in a future paper. A 25-cm-diameter metal ring was centered over each permeability sample location (as well as some additional localities), and every visible fracture trace inside the ring was measured. For each set of fracture orientations within the ring, representative true strike and dip were measured and recorded. Fracture data collected by the circular survey method only account for the portion of the exposure sampled for gas permeability (i.e., between 14.92 m and 30.90 m where $x = 0$ at the western end of the exposure). StereoStat™ Version 1.3 was used to plot all data.

Results

A total of 63 faults and 3173 fractures exposed at the Crucifix Site were measured and documented (Figure 3a). The orientations of the faults correspond to two conjugate sets (Figure 3b). The two sets have average orientations (strike/dip) of 182/75 (west dipping) and 352/69 (east dipping). The fracture data define three sets of fracture orientations (Figure 3c,d). The average orientations for the sets are 175/90 (vertical), 178/69 (west dipping), and 348/71 (east dipping).

Fault survey

The average fault pole orientation has an orientation (azimuth/plunge) of 266/04; therefore, the average extension direction is inferred to be 266°, which corresponds to the regional Basin and Range east-west extension direction observed in northern Owens Valley. The total fault heave across the exposure is 3.35 m. Correcting fault heave to extension-parallel heave yields 3.04 m of heave in the extension direction (Figure 4).

Faults are absent in the majority of the exposure, and faulting is concentrated in two zones at the western and eastern of the exposure (Figures 4 and 5). Plots of fault dip, fault-parallel displacement, and fault frequency as a function of position along the transect (Figure 5) illustrate the distribution of faults and the spatial heterogeneity in the fault system. Fault dip angles at the exposure have a maximum of 88° and a minimum of 41°, and the majority of values are between 60 and 85° (Figure 5a). The principal zones of displacement are at the western and eastern ends of the exposure (Figure 5b). Fault frequencies were calculated for bin sizes of 2 to 10 m, and the highest fault frequencies occur at the western end of the exposure (Figures 4 and 5c). Fault displacement versus fault core thickness data (Figure 6) show that the west and east dipping faults that bound the exposure have the greatest displacements (3.77 and 4.38 m, respectively) and relatively thick core zones (0.025 and 0.10 m, respectively). Three faults, however, have

much smaller displacements (0.38 m, 0.42 m, and 0.15 m), yet exhibit comparable core thicknesses (0.03 m, 0.05 m, and 0.02 m). This might occur because grain size, as well as displacement, controls fault zone thickness in these tuffaceous sedimentary rocks. All other faults in the exposure have less than 0.5 m displacement and range in thickness from 0.0005 to 0.01 m.

A plot of cumulative percent of faults (size distribution from small to large heave) versus cumulative percent of extension-parallel heave (Figure 7) shows that a small portion of the total fault population accommodates a large portion of the total heave (20% of the faults account for 92% of the total extension observed in the exposure). Although the majority of the total strain is borne by the two horst-bounding faults, a small component of extensional strain has been distributed into the surrounding rock.

Fracture survey

Data from 140 circular sample surveys performed at the western end of the exposure include measurements of 3173 fractures, 42 faults, and 200 sets of true strike and dip orientations. Two distinctive fracture patterns are observed in the exposure—a vertical fracture set and two sets of oppositely dipping steep but nonvertical (conjugate) fractures (Figure 3c,d). Data show that vertical fractures predominate in the nonfaulted areas of the exposure, whereas the nonvertical fractures dominate in the highly faulted areas (Figures 8 and 9). Fracture density (cm/cm^2) was determined by dividing total fracture trace length by the circular area for each set. Figure 3d illustrates fracture density as a function of fracture dip and shows the range of densities for both the vertical (90° dips) and nonvertical ($<90^\circ$ dips) fracture sets. Analyses of true fracture orientations as a function of location in the exposure (Figure 8, 9) show that vertical fractures are consistently present, although not uniformly developed, throughout the exposure. The distribution of nonvertical fractures is more sporadic, with the greatest concentration occurring in a highly faulted section between 15 and 21 m and in a nonfaulted section between 29 and 31 m at the west end of the exposure. Of the 3173 fractures mapped at the Crucifix Site, 2354 were vertical and 819 were nonvertical. Fracture length is represented by line diagrams showing the total fracture length as a proportionally-scaled line oriented in the dip orientation of the fracture set, as seen in a vertical (dip parallel) profile (Figure 9a,b). The line diagrams are plotted above (upper bed) and below (lower bed) their location on the photomosaic and illustrate the fracture distribution described above.

Fault zone deformation

Caine et al. (1996) describe an upper-crustal fault zone model that contains three components: a central fault core (containing slip surfaces, gouge zones, chemically altered zones, or cataclastic zones), a damage zone surrounding the fault core (containing small faults, veins, fractures, and/or folds), and the undeformed protolith (where fault-related structures are absent).

Fault zones at the Crucifix Site have unique geometries depending on the amount of displacement and the grain size of the faulted bed (Figures 6 and 10). The centimeter-scale (Figure 10a,b) and sub-centimeter-scale displacement faults at the Crucifix Site contain distinct slip surfaces with no discernible core or damage zone. The decimeter-scale displacement faults (Figure 10c) have distinct slip surfaces, but unlike the smaller faults, these have a small fault core and a damage zone. Cataclasis and postdepositional crystallization are observed along the fracture planes of some of the smaller faults (Figure 10c). The two meter-scale displacement faults (Figure 10d,e) have all three components of the Caine et al. (1996) model. More specifically they each have a measurable central fault core, a distinct damage zone, and an undeformed protolith.

The two bounding faults have fault cores that are composed of fine-grained comminuted material. Fault core thicknesses vary depending on the grain size of the bed encountered by the fault. Coarser-grained beds produce thicker fault cores, whereas finer-grained beds produce noticeably thinner fault cores. The two bounding faults have cores that are defined by and contain slip surfaces. Most of the associated deformation created by these two faults is observed within the damage zone of the footwall. The damage zone is composed of small, centimeter scale, conjugate faults and fractures that form a cluster within 1 to 2 m of the large faults. The western bounding fault has a highly deformed footwall that extends 2 m to the east. Across this distance there are 25 measurable fault traces and both nonvertical and vertical fractures. The hanging wall of the western bounding fault has no associated faults and only subvertical fractures that span a few centimeters away from the fault. The eastern bounding fault has a slightly different damage zone (i.e., the deformation spans just over 1 m in the footwall) with eight identifiable fault traces and numerous nonvertical fractures. The hanging wall of this fault is deformed by five small (< 10 cm displacement) faults and nonvertical fractures across a distance of 0.5 m. The protolith for each bounding fault is the undeformed section of rock just outside the damage zone.

Interpretation of stress history

Deformation at the Crucifix Site is manifest as vertical fractures and conjugate faults and fractures (Figure 11). These deformation features are controlled by differential stress, effective minimum principal compressive stress, and the strength characteristics of the rock (Hancock, 1985; Mandl, 1988; Engelder, 1993; Ferrill and Morris, 2003; Ferrill et al., 2004). Figures 12 and 13 depict the interpreted stress history at this exposure. As described in detail below, we interpret that (i) shear fractures formed during conditions of maximum overburden shortly after Bishop Tuff deposition, (ii) hybrid fractures formed during the transition between shear and tensile failure, and (iii) tensile fractures formed under conditions of low overburden stress (near zero) during erosion of the overburden by downcutting of the Owens River.

There are three possible failure modes within naturally occurring rocks: shear, tensile, and hybrid (e.g., Mandl, 1988; Ferrill and Morris, 2003). Shear failure is characterized by the formation of a fracture with displacement parallel to the fracture surface. Tensile failure is characterized by the formation of a fracture with displacement perpendicular to the fracture surface. Hybrid failure is characterized by the formation of a fracture with displacement oblique to the fracture surface. Hybrid failure occurs during the transition between shear and tensile failure and requires a tensile minimum principal compressive stress (σ_3 , where the maximum, intermediate and minimum principal compressive stresses are defined: $\sigma_1 \geq \sigma_2 \geq \sigma_3$ respectively). Shear failure surfaces in brittle, less competent rocks have lower angle dips in the range of 45 to 75°, whereas hybrid failure surfaces in the same rocks have dips that range from 75 to 90° (Mandl, 1988; Ferrill and Morris, 2003). The range of fault dips at this exposure is between 41 and 88°. Fault slip surfaces with dips in the range of 41 to 75° (approximately 50% of observed faults) are likely shear mode failure surfaces. The vertical fractures at this location are interpreted to be mode 1 tensile fractures. The large population of steep, nonvertical, conjugate-style fractures and fault surfaces with dips >75° are interpreted as evidence of hybrid failure. Fault and fracture geometries at the Crucifix Site show that all three failure modes have occurred.

Rock strength test data are needed to construct failure envelopes (Hoek and Brown, 1980). Because no such tests have been performed on the Crucifix Site sediments, data from an analogous rock type at Yucca Mountain, Nevada, were used. The Crucifix Site sediments contain clast-supported bedded deposits and textural, structural, and hydrological characteristics that are similar to the PTn and the nonwelded

Bishop Tuff (Fedors et al., 2001; Dinwiddie et al., 2002). Therefore, data produced from rock strength tests on the PTn were used to construct a failure envelope for this study. Three variables must be defined to construct a Hoek-Brown failure envelope:

- m = material constant for the rock mass
- s = constant which depends upon the rock mass characteristics
- c = uniaxial compressive strength of the intact rock pieces

A value of 17.64 was used from the m constant of the Tiva Canyon nonwelded unit of the PTn (CRWMS M&O, 2000b). Hoek and Brown (1980) give a range between 0 and 1 for the s constant, and it is suggested that a value of 1 be given for intact rock. Rock at the Crucifix Site is not intact, so the s value was inferred based on (i) the observed presence of vertical fractures, (ii) the poorly indurated Crucifix Site sediments, and (iii) the maximum vertical principal stress of 2.51 MPa (Table 1). We considered a range of values from 0.21 to 0.38 and found 0.3 to be reasonable. For the uniaxial compressive strength (c) of these rocks, a value of 7.31 MPa was assumed, which is the average value from several unconfined compressive strength tests performed on samples of the PTn (Bechtel SAIC Company, LLC, 2003b). A derived failure envelope for rocks at the Crucifix Site based on these data is illustrated in Figure 13.

When the Crucifix Site sediments were deposited, vertical stress (σ_1) would have been negligible (Figures 12 and 13a). We present a possible sequence of events below to illustrate deformation during the progressive burial and exhumation. First, lithification of the tuffaceous sediments would begin. Vertical stress may have increased because burial increased. Ongoing tectonic extension would have generated a differential stress with σ_3 oriented approximately east-west (Figures 12 and 13b). Conditions suitable for tensile (mode 1) failure are likely to develop. Second, at 0.76 Ma, the deposition of the Bishop Tuff imposed a greater lithostatic stress state on the Crucifix Site sediments. Assuming the thickness and density profiles (Wilson and Hildreth, 2003) of the overlying Bishop Tuff and Crucifix Site sedimentary rock given in Table 1, the lithostatic stress acting on the tuffaceous sedimentary deposit was estimated to be between 2.24 and 2.78 MPa (average 2.51 MPa; Table 1; Figures 12 and 13c). Third, continuous tectonic extension decreased σ_3 (Figure 13). The faults with moderate dips (between 41 and 75°) observed at the Crucifix Site are evidence of shear failure, and it is most likely that shear failure conditions were attained shortly after the emplacement of the Bishop Tuff when a decreasing σ_3 and an approximately constant σ_1 generated sufficient differential stress to reach the failure envelope (Figures 12 and 13c). Fourth, gradual erosion of the Bishop Tuff would have caused a decrease in σ_1 ; continuous tectonic extension and the decrease in lithostatic pressure would have generated a tensile σ_3 (Figures 12 and 13d). Conditions for hybrid failure, as indicated by nonvertical fractures and faults steeper than 75°, would have occurred. Continued removal of overburden and the subsequent decrease in lithostatic stress, in addition to continuous tectonic extension would ultimately create conditions under which simple tensile failure (vertical fracturing) could occur (Figures 12 and 13e). Tensile mode 1 fractures at the Crucifix Site developed best where no previous fractures (that could be reactivated) existed.

Discussion

The Crucifix Site sediments are cut by approximately north-south trending conjugate faults ranging in displacement from 0.002 to 4.4 m having dips ranging from 41 to 88°. Faults are not evenly distributed through the 110 m of exposure, but, rather, are clustered at the western and eastern margins forming a broad horst.

Fractures showing no evidence of shear displacement occur as three sets: two with north-south strike and opposite dips (range between 35 and 88°) and a vertical set

also with north-south strike. Nonvertical fractures are strongly clustered near fault zones, whereas vertical fractures occur throughout the entire exposure, although they are not evenly distributed.

Compared to previously discussed research of deformation characteristics within poorly lithified rocks (Heynekamp et al., 1999; Davatzes and Aydin, 2003; Davatzes et al., 2003; Wilson et al., 2003; Flodin and Aydin, 2004; Odling et al., 2004), the Crucifix Site sediments are extremely weak and poorly lithified. Many of the features discussed in previous studies, however, are also found in these sediments. Some of the faults at the Crucifix Site have distinct slip surfaces at the mesoscopic level, and others have characteristics similar to deformation bands described by Wilson et al. (2003) and Heynekamp et al. (1999). The Crucifix Site faults that resemble deformation bands also exhibit grain size reduction and cataclasis. These faults commonly show centimeter-scale displacements and form in clusters near the larger-displacement faults. This association is similar to the cluster zones discussed by Odling et al. (2004). The two bounding faults at the Crucifix Site have a similar geometry to faults described by Heynekamp et al. (1999). These faults have a core zone that contains the main slip surfaces; a mixed zone that extends a few centimeters on either side of the fault and that contains irregular slip surfaces and comminuted material; and a damage zone that is mostly confined to the footwall side of the faults. The damage zone typically contains a cluster of subsidiary faults and fractures that resemble both deformation bands and simple fractures. Fault core zones of the two bounding faults vary in thickness on the order of a few centimeters and as a function of grain size. This variation as the faults cut through different beds may indicate that the fault core zone thickness varies as a function of protolith grain size. A possible explanation for this relationship is that in coarser-grained beds, strain hardening causes thicker fault cores than in finer-grained material, in which strain softening occurs. In both cases intrinsic permeability is decreased by grain comminution and pore collapse in the coarser-grained material, and by clay smear process in the finer-grained material.

Two different scenarios may explain the faulting and fracturing at the Crucifix Site within the context of the interpreted stress history: (1) vertical fractures occurred first and were overprinted by the conjugate faults and fractures during maximum burial and were further overprinted by vertical fractures as the overburden decreased, or (2) conjugate faults and fractures occurred first and were overprinted by vertical fractures as the overburden diminished to its current state. Although cross-cutting relationships between faults are readily discernable, definitive evidence of cross-cutting relationships among fractures is generally lacking.

Deformation features within these tuffaceous sediments are likely to strongly influence permeability and fluid flow. Deformation at the Crucifix Site produced a very high density of fractures and small-displacement faults that are localized around larger displacement faults. Extension fractures potentially produce larger open porosity than in the host material, whereas cataclastic deformation within fault zones produces grain size and pore size reduction. The influence of these deformation processes on water movement depends on the saturation conditions. Under saturated conditions, the open fractures would tend to serve as conduits, and the cataclastic fault zone material with smaller pore sizes would tend to act as barriers. Under unsaturated conditions, moisture may wick into and be retained in the fine-grained fault zones due to capillary forces, and open extension fractures may act as barriers because of moisture retention in the smaller pores of the adjacent host rock. Ponded infiltration tracer tests in the nonwelded Bishop Tuff, which has a high capillary wicking potential, showed that a highly deformed section of rock with vertical and subvertical fractures enhanced vertical flow by laterally constraining the flow paths (Fedors et al., 2001). Under these locally saturated conditions, the fractures, which are partially cemented with caliche-like cement, did not

act as conduits, but rather as boundaries that defined preferential flow blocks. Regardless of the saturation conditions, deformation features like those analyzed at the Crucifix Site influence potential fluid pathways and produce permeability anisotropy in the faulted and fractured strata.

The work described in this paper was performed as an analog study that would contribute to a conceptual understanding relevant to flow models for the PTn at Yucca Mountain, Nevada. Although the clast-supported tuffaceous sediments of the Crucifix Site differ in lithologic detail from the PTn, the structural characteristics observed at the Crucifix Site are similar. The PTn is exposed in the walls of the Exploratory Studies Facility tunnel at Yucca Mountain (CRWMS M&O, 1998). Detailed line survey data for the nearly-horizontal tunnel (CRWMS M&O, 1998) document that fault frequencies (the number of faults per meter of tunnel) range from 0.16 faults per meter in the north ramp to 0.50 faults per meter in the south ramp within the PTn designated horizons, comparable to the fault frequency at the Crucifix site (0.57 faults per meter). Understanding the effect that the deformation characteristics within the Crucifix Site sediments have on intrinsic permeability provides a conceptual model and analog for defining the role that deformation has on permeability architecture. Furthermore, developing the history of stratal accumulation, erosion, and deformation yields a better understanding of the *in-situ* stress. This technical approach, for example, could prove helpful in improving the understanding of the evolution of lithologic properties, stress history, and deformation of various units at Yucca Mountain.

Conclusions

After deposition, the tuffaceous sedimentary rocks at the Crucifix Site underwent a period of shear, hybrid, and up to two episodes of tensile failure that produced the observed pattern of conjugate faults and fractures, both vertical and nonvertical. Two oppositely dipping normal faults on the exposure form a horst. These two faults account for 75% of the total extension-parallel heave. Stress analysis based on overburden estimation suggests that low differential stress (of the order of 2.5 MPa) with a near-zero minimum principal stress produced the observed deformation.

The Crucifix Site exposure contains some of the least lithified tuffaceous sediments for which rock failure has been studied. The level of consolidation, however, does not prevent these rocks from preserving a set of deformation features that are very similar to those observed in studies of high porosity sandstones, other poorly lithified siliciclastic rocks, and nonwelded tuffs. These features include (i) cataclastic shear deformation and extension fracturing, (ii) variations in fault zone thickness and geometry controlled by lithology, (iii) clusters of small displacement faults and fractures that form near larger displacement faults, and (iv) the overprinting of different failure modes and deformation mechanisms.

Deformation features influence the intrinsic permeability of the system. Fault zone deformation commonly involves grain size and pore volume reduction resulting in reduced permeability. Under unsaturated conditions, the smaller mean pore size produces an increased capillary (wicking) effect in addition to reduced permeability. A fault system such as this would influence fluid flow both vertically and laterally. Vertical fluid movement would be focused down dip and lateral fluid movement would be restricted horizontally by the faults that behave as flow barriers. Influences such as these would potentially enhance fluid flow in a direction parallel to the intersection line of conjugate faults. The fault system will influence groundwater movement under both saturated and unsaturated conditions. This influence may differ, however, with open

faults and fractures acting as conduits under saturated conditions and barriers under unsaturated conditions.

Acknowledgments

This paper was prepared to document work performed by the Center for Nuclear Waste Regulatory Analyses (CNWRA) for the U.S. Nuclear Regulatory Commission (NRC) under Contract No. NRC-02-02-012. The activities reported here were performed on behalf of the NRC Office of Nuclear Material Safety and Safeguards, Division of High-Level Waste Repository Safety. This paper is an independent product of CNWRA and does not necessarily reflect the views or regulatory position of NRC.

The authors would like to thank Brittain Hill and Goodluck Ofoegbu for providing technical assistance. The authors are grateful to Robert Smith, Kevin Smart, Brittain Hill, John Stamatakos, Gary Walter, and Gordon Wittmeyer for technical reviews, and to Paulette Houston and Erika Hanson for their editorial help in preparing the manuscript.

References

- Bateman, P.C., 1965. Geology and tungsten mineralization of the Bishop district California. U.S. Geological Survey Professional Paper 470.
- Bechtel SAIC Company, LLC, 2001. FY01 Supplemental Science and Performance Analysis. Volume 1. Scientific Bases and Analyses. TDR-MGR-MD-000007. Rev. 00, ICN01. Las Vegas, Nevada.
- Bechtel SAIC Company, LLC, 2003a. Abstraction of Drift Seepage. MDL-NBS-HS-000019. Rev.01. Las Vegas, Nevada.
- Bechtel SAIC Company, LLC, 2003b. Subsurface geotechnical parameters report. 800-K0C-WIS0-00400-000-00A. Las Vegas, Nevada.
- Caine, J.S., Evans, J.P., Forster, C.B., 1996. Fault zone architecture and permeability structure. *Geology* 24, 1025–1028.
- CRWMS M&O 1998. Geology of the Exploratory Studies Facility Topopah Spring Loop. BAB000000-01717-0200-00002, Rev. 01.
- CRWMS M&O, 2000a. Unsaturated zone flow and transport model PMR. TDR-NBS-HS-000002. Rev 00. Las Vegas, Nevada. Civilian Radioactive Waste Management System Management and Operating Contractor.
- CRWMS M&O, 2000b. Yucca Mountain Site Description. TDR-CRW-GS-000001 REV 01 ICN 01. Las Vegas, Nevada: CRWMS M&O. MOL.20001003.0111. Available: <<http://lsnnet.gov>> LSN accession No. NRC000025926.
- Davatzen, N.C., Aydin, A., Eichhubl, P., 2003. Overprinting faulting mechanisms during the development of multiple fault sets in sandstone, Chimney Rock fault array, Utah. *Tectonophysics* 363, 1–18.
- Davatzen, N.C., Aydin, A., 2003. Overprinting faulting mechanisms in high porosity sandstones of SE Utah. *Journal of Structural Geology* 25, 1795–1813.
- Dawers, N. H., Anders, M.H., Scholz, C.H., 1993. Growth of normal faults: displacement-length scaling. *Geology* 21, 1107–1110.
- Dawers, N. H., Anders, M.H. 1995. Displacement-length scaling and fault linkage. *Journal of Structural Geology* 17, 607–614.
- Day, W.C., Dickerson, R.P., Potter, C.J., Sweetkind, D.S., San Juan, C.A., Drake, II,

- R.M., Fridrich, C.J., 1998a. Bedrock geologic map of the Yucca Mountain area, Nye County, Nevada. U.S. Geological Survey Miscellaneous Investigations Series Map I-2627, scale 1:24,000.
- Day, W.C., Potter, C.J., Sweetkind, D.S., Dickerson, R.P., San Juan, C.A., 1998b. Bedrock geologic map of the Central Block Area, Yucca Mountain, Nye County, Nevada. U.S. Geological Survey Miscellaneous Investigations Series Map I-2601, scale 1:6000.
- Dinwiddie, C., Fedors, R., Ferrill, D.A., and Bradbury, K.K., 2002. *In-Situ* Measurement of Permeability in the vicinity of faulted nonwelded Bishop Tuff. EOS, Transactions of the American Geophysical Union, 2002 Fall Meeting Supplement, Abstract T21A-1069.
- Dinwiddie, C.L., Bradbury, K.K., McGinnis, R.N., Fedors, R.W., Ferrill, D.A., in review. Fault zone deformation overprints permeability of nonwelded ignimbrite: Chalk Cove fault, Bishop Tuff, Bishop, California. *Vadose Zone Journal*.
- Engelder, T., 1993. Stress regimes in the lithosphere. Princeton University Press, Princeton, NJ.
- Evans, J.P., Bradbury, K.K., 2004. Faulting and fracturing of nonwelded Bishop Tuff, Eastern California: deformation mechanisms in very porous materials in the Vadose Zone. *Vadose Zone Journal* 3, 602–623.
- Evans, J.P., 1990. Thickness-displacement relationships for fault zones. *Journal of Structural Geology* 12, 1061–1065.
- Fedors, R.W., Evans, J., Or, D., Forster, C., Heath, J., Bradbury, K.K., 2001. Unsaturated flow through fractured and unfractured non-welded tuffs. American Geophysical Union Fall Meeting, San Francisco, California,. Supplemental Abstract 82(47), H52A-0365.
- Fedors, R.W., Ferrill, D.A., 2002. Potential for lateral flow associated with fractured, nonwelded, layered tuffs in the unsaturated zone. EOS Transactions of the American Geophysical Union, 2002 Fall Meeting Supplement, Abstract H52B.
- Ferrill, D.A., Morris, A., 2001. Displacement gradient and deformation in normal fault systems. *Journal of Structural Geology* 23, 619–638.
- Ferrill, D.A., Morris, A., 2003. Dilational normal faults. *Journal of Structural Geology* 25, 183–196.
- Ferrill, D.A., Morris, A., Jones, S.M., Stamatakis, J.A., 1998. Extensional layer—parallel shear and normal faulting. *Journal of Structural Geology* 20, 355–362.
- Ferrill, D.A., Stamatakis, J.A., Sims, D., 1999. Normal fault corrugation: implications for growth and seismicity of active normal faults. *Journal of Structural Geology* 21, 1027–1038.
- Ferrill, D.A., Morris, A., Stamatakis, J.A., Sims, D., 2000. Crossing conjugate normal faults. *AAPG Bulletin* 84(10), 1543–1559.
- Ferrill, D.A., Morris, A., Wyrick, D.Y., Sims, D.W., Franklin, N.M., 2004. Dilational fault slip and pit chain formation on Mars. *GSA Today* 14, 4–12.
- Flodin, E., Aydin, A., 2004. Faults with asymmetric damage zones in sandstone, Valley of Fire State Park, southern Nevada. *Journal of Structural Geology* 26, 983–988.
- Gilbert, C.M., 1938. Welded tuff in eastern California. *Geological Society of America Bulletin* 49, 1828–1862.
- Hancock, P.L., 1985. Brittle microtectonics: Principles and practice. *Journal of Structural Geology* 7, 437–457.
- Heynekamp, M.R., Goodwin, L.B., Mozley, P.S., Haneburg, W.C., 1999. Controls on fault-zone architectures in poorly lithified sediments, Rio Grande Rift, New Mexico: implications for fault-zone permeability and fluid flow. *American*

- Geophysical Union, Geophysical Monograph 113, 27–49.
- Hildreth, E.W., 1979. The Bishop Tuff: Evidence for the origin of compositional zonation in silicic magma chambers, in ash flow tuffs. In: Chapin, C.E., Elston, W.E., Special Paper Geological Society of America 180, 43–75.
- Hildreth, W., Mahood, G.A., 1986. Ring-fracture eruption of the Bishop Tuff. Geological Society of America Bulletin 97, 396–403.
- Hoek, E., Brown, E.T., 1980. Underground excavations in rock. Institution of Mineral Metallurgy, London, England.
- Izett, G.A., Obradovich, J.D., Mehnert, H.H., 1988. The Bishop ash bed and some older chemically and mineralogically similar ash beds in California, Nevada, and Utah. U.S. Geological Survey Bulletin 1675, 37.
- Knott, S.D., Beach, A., Brockbank, P.J., Brown, J.L., McCallum, J.E., Welbon, A.I., 1996. Spatial and mechanical controls on normal fault populations. Journal of Structural Geology 18, 359–372.
- Lueddecke, S.B., Pinter, N., Gans, P., 1998. Plio-Pleistocene ash falls, sedimentation, and range-front faulting along the White-Inyo Mountains front, California. Journal of Geology 106, 511–522.
- Mandl, G., 1988. Mechanics of tectonic faulting. Elsevier, New York.
- Mayo, E.B., 1934. The Pleistocene Long Valley Lake in eastern California. Science, 80, 95–96.
- Metz, J., Mahood, G.A., 1985. Precursors to the Bishop Tuff eruption: Glass Mountain, Long Valley, California. Journal of Geophysical Research 90, 111,121–111,126.
- Morris, A.P., Ferrill, D.A., 1999. Constant-thickness deformation above curved normal faults. Journal of Structural Geology 21, 67–83.
- Moyer, T. C., Geslin, J. K., Flint, L. O., 1996. Stratigraphic relations and hydrologic properties of the Paintbrush Tuff Nonwelded (PTn) hydrologic unit, Yucca Mountain, Nevada. United States Geological Survey Open-File Report 95-397, 151pp.
- Odling, N.E., Harris, S.D., Knipe, R.J., 2004. Permeability scaling properties of fault damage zones in siliclastic rocks. Journal of Structural Geology 26, 1727–1747.
- Ofoegbu, G.I., Ferrill, D.A., 1998. Mechanical analyses of listric normal faulting with emphasis on seismicity assessment. Tectonophysics 284, 65–77.
- Pinter, N., 1995. Faulting on the Volcanic Tableland, Owens Valley, California. Journal of Geology 103, 73–83.
- Ragan, D.M., Sheridan, M.F., 1972. Compaction of the Bishop Tuff, California. Geologic Society of America Bulletin, 83, 95–106.
- Riehle, J.R., Miller, T.F., Bailey, R.A. 1995. Cooling, degassing, and compaction of rhyolitic ash flow tuffs: A computational model. Bulletin of Volcanology 57, 319–336.
- Rockware Inc., 2004. Rockware StereoStat® version 1.3, Golden, CO.
- Ross, C.S., Smith, R.L. 1961. Ash-Flow Tuffs: Their origin, geologic relations and identification. U.S. Geological Survey Professional Paper 366.
- Sarna-Wojcicki, A., Pringle, M.S., Wijbrans, J., 2000. New $^{39}\text{Ar}/^{40}\text{Ar}$ age of the Bishop Tuff from multiple sites and sediment rate calibration for the Matuyama-Bruhnes boundary. Journal of Geophysical Research 105(21), 431–21, 443.
- Schultz, R.A., Fossen, H., 2002. Displacement-length scaling in three dimensions: the importance of aspect ratio and application to deformation bands. Journal of Structural Geology 24, 1389–1411.
- Sheridan, M.F., 1970. Fumarolic mounds and ridges of the Bishop Tuff, California. Geological Society of America Bulletin 81, 851–868.

- Smith, R.L., 1960. Zones and zonal variations in welded ash flows. U.S. Geological Survey Professional Paper 354F, 149–159.
- Smith, G.A., 1986. Coarse-grained nonmarine volcanoclastic sediment: terminology and depositional process. Geological Society of America Bulletin 97, 1–10.
- Stewart, S.A., Reeds, A., 2003. Geomorphology of kilometer-scale extensional fault scarps: Factors that impact seismic interpretation. AAPG Bulletin 87, 251–272.
- Willemse, E.J.M., Pollard, D.D., Aydin, A., 1996. Three-dimensional analyses of slip distributions on normal fault arrays with consequences for fault scaling. Journal of Structural Geology 18, 295–309.
- Willemse, E.J.M., 1997. Segmented normal faults: Correspondence between three-dimensional mechanical models and field data. Journal of Geophysical Research 102(B1), 675–692.
- Wilson, C.J.N, Hildreth, W. 1997. The Bishop Tuff: New insights from eruptive stratigraphy. The Journal of Geology 105, 407–439.
- Wilson, C.J.N, Hildreth, W. 1998. Hybrid fall deposits in the Bishop Tuff, California: A novel pyroclastic depositional mechanism. Geology 26(1), 7–10.
- Wilson, C.J.N, Hildreth, W. 2003. Assembling an ignimbrite: Mechanical and thermal building blocks in the Bishop Tuff, California. Journal of Geology 111, 653–670.
- Wilson, J.E, Goodwin, L.B., Lewis, C.J., 2003. Deformation bands in nonwelded ignimbrites: Petrophysical controls on fault-zone deformation and evidence of preferential fluid flow. Geology 31(10), 837–840.
- Wu, Y.-S., Zheng, W., Pan, L., Hinds, J., and Bodvarsson, G.S., 2000. Capillary barriers in unsaturated fractured rocks of Yucca Mountain, Nevada. LBNL-46876. Berkeley, California, Lawrence Berkeley National Laboratory.

Table Title:

Table 1. Summary of thickness, density, and stress ranges for a section of the Bishop Tuff located near the Crucifix Site. Thickness and density values were taken from Wilson and Hildreth (2003).

Figure Captions:

Figure 1. (a) Physiographic map showing location of study area and surrounding features. Shaded-relief map generated from USGS 7½ minute quad DEMs, UTM zone 11, NAD 27. Resolution is 10 m. (b) Aerial photograph looking north across the southern boundary of the Volcanic Tableland illustrating Crucifix Site study area.

Figure 2. (a) Block diagram depicting the conceptual framework of deformation and overburden studied at the Crucifix Site. (b) Illustration of the stratigraphic evolution of the Crucifix Site.

Figure 3. Lower hemisphere, equal area projection of poles to fault and fracture surfaces measured at the Crucifix Site. (a) All fault and fracture data. Many of the faults and fractures have identical orientations. (b) West and east dipping fault orientations and the average extension direction. (c) West and east dipping and vertical fracture orientations. (d) Scatterplot of fracture density and fracture dip.

Figure 4. Plan view map of the Crucifix Site shows data used to calculate extension. The red arrows represent the two extension parallel lengths (L_I). The blue lines represent the

two bounding faults; the ball and bar are on the down-thrown side of the fault. Fault clusters are represented by boxes superimposed on the map. The blue arrow represents the extension-parallel heave (ΔL) for the entire exposure.

Figure 5. Three scatterplots illustrate the spatial distribution of fault properties along the transect. (a) The spatial distribution of fault dip angle. (b) The spatial distribution of fault displacement (measured as observed offset). (c) The spatial distribution of fault frequency (calculated as number of faults per meter at one meter intervals for 2, 4, 6, 8, and 10 m bin sizes).

Figure 6. A semi-log scatterplot illustrates the relationship between the thickness of fault cores and the corresponding fault displacements.

Figure 7. A scatterplot of cumulative percent extension-parallel heave versus cumulative percent of faults (ordered size distribution from small to large extension-parallel heave). Twenty percent of the faults account for ninety-two percent of the total extension.

Figure 8. A scatterplot and photomosaic illustrate the distribution of fracture strike azimuth, dip angle, and fracture density for vertical and nonvertical fractures. Vertical fractures occur consistently throughout this section of outcrop. The blue lines on the photomosaic represent fault traces. The scale is marked as the distance from the west end of exposure.

Figure 9. A photomosaic of the exposure that was studied during the fracture survey illustrates sample locations and fracture set orientations; the scale is the same as for Figure 8. Sample locations are marked by red dots and have sample identification numbers. A line diagram is drawn for each sample location. Each red line represents a fracture set that occurs at that location; the line orientation represents dip, and its length represents total fracture length in that fracture set. (a) Photomosaic and line diagrams for exposure between 15 and 23 m along the transect. (b) Photomosaic and line diagrams for exposure between 23 and 31 m along the transect.

Figure 10. A series of fault zone photographs illustrate the variety of fault displacements at the Crucifix Site. The grey marker bed lies between bed 1 and bed 2 and is used in this figure to show offset. (a) A fault with centimeter-scale displacement and a single slip surface. (b) Two faults with centimeter-scale displacement, and the main fault has a series of associated slip surfaces exhibiting an en echelon pattern. (c) Two faults with decimeter-scale displacements. The fault cores become thicker with increased displacement and fracture frequency noticeably increases. (d) The west bounding fault with 3.76 m displacement. The west bounding fault has the greatest fault core thickness of all faults at the Crucifix Site, and the associated deformation is concentrated within the footwall block. (e) The east bounding fault with 4.37 m of displacement has the largest displacement of all faults at the Crucifix Site, and the associated deformation is observed on both sides of the fault.

Figure 11. (a) Block diagram from Figure 2a. (b) Block diagram illustrating deformation within the 20-m section of outcrop where the circular sample survey was performed. (c) Block diagram illustrating the deformation characteristics of a highly faulted portion of the exposure. (d) Block diagram illustrating the deformation characteristics near a non-faulted portion of the exposure. The color features are as follows; the orange bed is bed 1, the green bed is bed 2, the blue lines are faults, the black lines are fractures, and the

red horizontal line is the marker bed along which the fault scanline survey was performed.

Figure 12. Hypothesized stress evolution of the Crucifix Site sediments. The illustration shows the circumstances under which shear, tensile, and hybrid failure may have occurred at the Crucifix Site. The circled numbers mark points in time where the stress states shown in Figure 13 are expected to have occurred.

Figure 13. A series of Mohr-space diagrams illustrating the likely stress states that produced the deformation observed at the Crucifix Site. Hoek and Brown (1980) failure envelopes for the Crucifix Site sedimentary rock are shown on each diagram, and are color-coded according to fault dips and failure angles for the normal faulting regime. These diagrams illustrate the stress state under which all three failure modes (shear, tensile, and hybrid) are expected to have occurred.